Journal of Harbin Engineering University
ISSN: 1006-7043

Vol 45 No. 9
September 2024

Long Baseline Navic Relative Positioning with Simultaneous Estimation of Ionospheric and Tropospheric Delay and Gradients

[1]Goli Suresh Kumar*, [2]D. Krishna Reddy, [3]P. Naveen Kumar

[1]*Corresponding author: Research Scholar, Department of ECE, University College of Engineering, Osmania University, Hyderabad, India. Email: suresh.ece.uceou@gmail.com

[2]Professor, Department of Electronics and Communication Engineering, Chaitanya Bharathi Institute of Technology, Hyderabad, Telangana, India

[3]Professor, Department of ECE, University College of Engineering, Osmania University, Hyderabad, India

Abstract: Ionosphere and troposphere delays greatly impact position accuracy in long baseline NavIC/GNSS relative positioning. In this paper, we describe algorithms for relative position computation using Real Time data that simultaneously estimate troposphere and ionosphere delays and their gradients, and are optimized for long baselines. We also reenter various dynamical models of the rover station for Kalman filter use. Relative positioning experiment results for different baselines (short, medium, and long) are presented with NavIC data from four different receiver stations in India.

Keywords: NavIC; Relative Position; Ionospheric delay; Tropospheric delay

1. Introduction

As the ionosphere and troposphere delays show significant discrepancies between reference and rover receiver stations of NavIC/GNSS, conventional single and double difference approaches [1-3] become inadequate for medium and long baselines exceeding 20 kms. The authors developed innovative methods for long baseline relative positioning in order to overcome this difficulty. These algorithms integrate ionospheric delay and tropospheric delay as dynamic variables within a Kalman filter framework. By treating these delays and their gradients as state variables, the algorithms aim to swiftly and accurately estimate their variations across both reference and rover stations.

Earlier research modelled troposphere delays by splitting the overall delay into wet and zenith hydrostatic delays, which were then adjusted using mapping functions [4-5]. Zenith wet delay was considered as an adjustable parameter calculated during positional computations, while zenith hydrostatic delay was handled as an exact fit using the Saastamoinen model. Using an inhomogeneous mapping function, the current study expands on previous research by examining horizontal differences in troposphere delays inside the lower atmosphere. In order to minimize the horizontal components of troposphere delays and improve horizontal positioning accuracy, this function includes a first-order gradient to account for water vapour deformation. To mitigate ionosphere delays, several methods exist. On the other hand, the Klobuchar model, which peaks at 14:00 local time, depicts the zenith ionosphere delay as a half-cosine function during the day and a constant value at night. However, it only mitigates about 50% of the ionosphere delay Root Mean Square Error (RMS) [6]. The IGS (International GNSS Service) provides total electron content (TEC) of the ionosphere globally through its Global Ionosphere Model (GIM). This uses the same GPS dataset and ephemeris but produces better results than the Klobuchar model.

Similarly to the troposphere delay estimates, the authors also incorporate ionosphere effects into the positioning model [4-5]. At reference and rover stations, zenith delays and mapping functions are used, delays for all satellites are simulated. Zenith ionosphere delays are converted to slant delays using mapping functions. An inhomogeneous mapping function accounts for east and north horizontal gradients, with the Kalman filter employed to estimate ionosphere delays and horizontal gradients. This study assumes that both the horizontal gradients and zenith ionosphere delay adhere to a first-order Markov process or Brownian motion. The proposed long baseline relative positioning algorithms enable prompt and precise positioning by estimating ionosphere and troposphere delays along with their gradients. Experimental results are presented under various conditions, and different baseline lengths.

2. Mathematical Model

In this paper we consider the mathematical models that may be used to both static and kinematic position, for integrated pseudo range and carrier phase measurements involving a receiver (u) and a satellite (p). The consequent double-differenced pseudo ranges $\rho^{pq}_{CA,ku}$ and $\rho^{pq}_{PY,ku}$ are obtained when satellites *'p'* and *'q'* provide pseudo range and carrier phase readings to receiver's *'k'* and *'u'* respectively. Also, the double-differenced carrier phases $\phi^{pq}_{L5,ku}$, $\phi^{pq}_{S1,ku}$ based on L5 and S1 frequency bands are formulated as follows [7-9].

$$\rho^{pq}_{CA,ku}(t) = r^{pq}_{ku}(t) + \delta I^{pq}_{ku}(t) + \delta T^{pq}_{ku}(t) + e^{pq}_{CA,ku}(t) \quad (1)$$

$$\rho^{pq}_{PY,ku}(t) = r^{pq}_{ku}(t) + \frac{f_1^2}{f_2^2}\delta I^{pq}_{ku}(t) + \delta T^{pq}_{ku}(t) + e^{pq}_{PY,ku}(t) \quad (2)$$

$$\phi^{pq}_{L5,ku}(t) = r^{pq}_{ku}(t) - \delta I^{pq}_{ku}(t) + \delta T^{pq}_{ku}(t) + \lambda 1 N^{pq}_{L5,ku} + \lambda 1 \in^{pq}_{L5,ku}(t) \quad (3)$$

$$\phi^{pq}_{S1,ku}(t) = r^{pq}_{ku}(t) - \frac{f_1^2}{f_2^2}\delta I^{pq}_{ku}(t) + \delta T^{pq}_{ku}(t) + \lambda 2 N^{pq}_{S1,ku} + \lambda 2 \in^{pq}_{S1,ku}(t) \quad (4)$$

Where

$$\delta I^{pq}_{ku}(t) = \left(\delta I^{p}_{k} - \delta I^{p}_{u}\right) - \left(\delta I^{q}_{k} - \delta I^{q}_{u}\right) \quad (5)$$

$$\delta T^{pq}_{ku}(t) = \left(\delta T^{p}_{k} - \delta T^{p}_{u}\right) - \left(\delta T^{q}_{k} - \delta T^{q}_{u}\right) \quad (6)$$

$$N^{pq}_{L5,ku} = \left(N^{p}_{L5,k} - N^{p}_{L5,u}\right) - \left(N^{q}_{L5,u} - N^{q}_{L5,u}\right) \quad (7)$$

$$N^{pq}_{S1,ku} = \left(N^{p}_{S1,k} - N^{p}_{S1,u}\right) - \left(N^{q}_{S1,k} - N^{q}_{S1,u}\right) \quad (8)$$

$$e^{pq}_{CA,ku}(t) = \left(e^{p}_{CA,k} - e^{p}_{CA,u}\right) - \left(e^{q}_{CA,k} - e^{q}_{CA,u}\right) \quad (9)$$

$$e^{pq}_{PY,ku}(t) = \left(e^{p}_{PY,k} - e^{p}_{PY,u}\right) - \left(e^{q}_{PY,k} - e^{q}_{PY,u}\right) \quad (10)$$

$$\in^{pq}_{L5,ku} = \lambda 1\left[\left(\in^{p}_{L5,k} - \in^{p}_{L5,u}\right) - \left(\in^{q}_{L5,k} - \in^{q}_{L5,u}\right)\right] \quad (11)$$

$$\in^{pq}_{S1,ku} = \lambda 2\left[\left(\in^{p}_{S1,k} - \in^{p}_{S1,u}\right) - \left(\in^{q}_{S1,k} - \in^{q}_{S1,u}\right)\right] \quad (12)$$

In this context, 't' represents the signal reception time, while *f₁* and *f₂* denote the L5 and S1 carrier frequencies, specifically 1176.45 MHz and 2492.028 MHz respectively. The terms I_{ku} and T_{ku} correspond to the double-differenced ionosphere and troposphere propagation delays. The observation noises are represented by $\in^{pq}_{L5,ku}$, $\in^{pq}_{S1,ku}$. The uncertainty of the L5 and S1 carrier phases at the beginning time is linked to the unknown integer ambiguities, $N^{pq}_{L5,ku}$ and $N^{pq}_{S1,ku}$. The wavelengths of the L5 and S1 wave carriers are indicated by λ1 and λ2.

$r^{p}_{u}(t)$ denotes the distance from satellite *p* to receiver *u* at time t-τ_p and at time t, where τ_p represents the travel time of the carrier signal.

$$r^{pq}_{ku} = (r^{p}_{k} - r^{p}_{u}) - (r^{q}_{k} - r^{p}_{u})$$

$$= \left\{\begin{matrix}\sqrt{(x_k - x^1)^2 + (y_k - y^1)^2 + (z_k - z^1)^2} - \\ \sqrt{(x_u - x^1)^2 + (y_u - y^1)^2 + (z_u - z^1)^2}\end{matrix}\right\} - \left\{\begin{matrix}\sqrt{(x_k - x^q)^2 + (y_k - y^q)^2 + (z_k - z^q)^2} - \\ \sqrt{(x_u - x^q)^2 + (y_u - y^q)^2 + (z_u - z^q)^2}\end{matrix}\right\} \quad (13)$$

Consequently, the approximate value of $u^P = \hat{u}^p$ for the first-order Taylor sequence estimate of Formula (13) can be represented as follows:

$$r^{pq}_{ku} \approx r^{pq}_{k\hat{u}(j)} + \left[\frac{\partial r^{pq}_{ku}}{\partial u}\right]^2_{u=\hat{u}(j)} \left(u - \hat{u}(j)\right) = r^{pq}_{k\hat{u}(j)} + g^{pq}_{k\hat{u}(j)}\left(u - \hat{u}(j)\right) \quad (14)$$

In the context of short baselines, the ionosphere and troposphere delays present in the measurements are assumed to be nearly the same at both the reference and rover stations. This allows us to assume that:

$$\delta I^{pq}_{ku} \approx 0, \quad \delta T^{pq}_{ku} \approx 0, \quad (15)$$

Hence, equations (1) through (4) can be approximated in the following manner:

$$\rho^{pq}_{CA,ku}(t) \approx r^{pq}_{ku}(t) + e^{pq}_{PY,ku}(t) \quad (16)$$

$$\rho^{pq}_{PY,ku}(t) \approx r^{pq}_{ku}(t) + e^{pq}_{PY,ku}(t) \quad (17)$$

$$\phi^{pq}_{L5,ku}(t) \approx r^{pq}_{ku}(t) + \lambda 1 N^{pq}_{L5,ku} + \lambda 1 \in^{pq}_{L5,ku}(t) \quad (18)$$

$$\phi^{pq}_{S1,ku}(t) \approx r^{pq}_{ku}(t) + \lambda 2 N^{pq}_{S1,ku} + \lambda 2 \in^{pq}_{S1,ku}(t) \quad (19)$$

Nevertheless, during medium or long baseline scenarios, it is not feasible to rely on the assumptions presented in Equation (15). Failure to properly eliminate ionosphere and troposphere delays from double difference measurements poses a risk of degrading positioning accuracy. Hence, we introduce long baseline relative positioning algorithms, leveraging Equations (1)-(4). We employ parametric frameworks for troposphere delay and compute ionosphere delays as state variables simultaneously at reference and rover sites.

3. Tropospheric Delay Models:

3.1 A Review of Approaches Analyzing Hydrostatic and Wet Delays:

The troposphere delay is a major factor for low-altitude satellites. The troposphere imposes equal delays across many frequencies, in contrast to the ionosphere, which displays dispersive features. The wet delay and the hydrostatic delay are the two main parts of the troposphere delay. Because the wet delay accounts for 10% of the total troposphere delay, modelling it is difficult because of local fluctuations in the troposphere water vapor content. On the other hand, 90% of the troposphere delay is made up of the hydrostatic delay, which is more accurately modelled [4]. The zenith hydrostatic delay (ZHD), shown as $\delta T_{zh,u}$, and the zenith wet delay (ZWD), shown as $\delta T_{zw,u}$ can be added to provide the zenith total troposphere delay (ZTD), abbreviated as STz. Figure 1 provides an illustration of this relationship [7,10].

$$\delta T_{z,u} = T_{zh,u} + \delta T_{zw,u} \qquad (20)$$

Subsequently, the total slant delay can be described by employing mapping functions in the following manner:

$$\delta T_u^p = M_{h,u}^p \delta T_{zh,u} + M_{w,u}^p \delta T_{zh,u} \qquad (21)$$

$$M_{h,u}^p = \frac{1}{\sin\left(E_u^p\right) + \frac{0.00143}{\tan\left(E_u^p\right)+0.0445}} \qquad (22)$$

$$M_{w,u}^p = \frac{1}{\sin\left(E_u^p\right) + \frac{0.00305}{\tan\left(E_u^p\right)+0.017}} \qquad (23)$$

E_u^p denotes the elevation angle of the p-th satellite, while $M_{h,u}^p$ and $M_{w,u}^p$ stand for the mapping values for the hydrostatic and wet elements. The Saastamoinen model is then used to calculate the zenith hydrostatic delay.

$$\delta T_{zh,u} = 0.002277(1 + 0.0026 cos 2\emptyset_u + 0.00028 h_u) P_0 \qquad (24)$$

The latitude and altitude of the receiver's position are denoted by $\emptyset_u$ and h_u [km], respectively, while P_0 [mbar] represents the atmospheric pressure. Furthermore, it is thought that the zenith total delay is an unknown parameter.

3.2 Tropospheric gradients

When utilizing data from low elevations, the horizontal troposphere delay's variability becomes more significant, leading to challenges in precise positioning. Neglecting this variation may result in relatively substantial errors in the positioning outcomes.

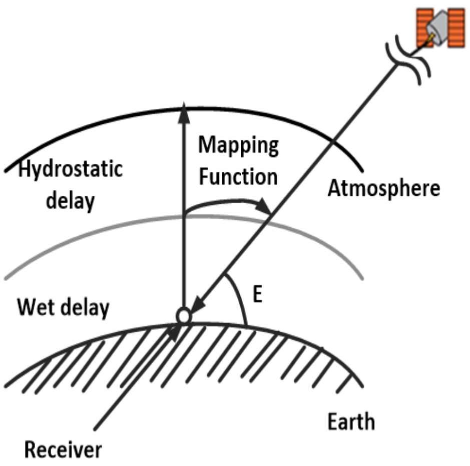

Figure1: Troposphere delay mapping function

Consequently, this study applies the horizontal deformation of the tropospheric delay to estimate tropospheric delays. Subsequently, tropospheric gradients are estimated and corrected using mapping functions. The delay in the NavIC signal caused by the tropospheric gradient can be represented as follows:

$$\delta T_G\left(E_u^p, A_u^p\right) = \delta T_{ns} M_{T_a}\left(E_u^p\right) cos A_u^p + \delta T_{ew} M_{T_a}\left(E_u^p\right) sin A_u^p \qquad (25)$$

Where,

$$M_{T_a}\left(E_u^p\right) = \frac{1}{sin E_u^p tan E_u^p + 0.0032} \qquad (26)$$

Here, δT_{ns} and δT_{ew} represent the gradients in the north-south and east-west directions, respectively. A_u^p denotes an azimuth, and

$M_{T_a}(E_u^p)cosA_u^p, M_{T_a}(E_u^p)sinA_u^p$ are the inhomogeneous mapping functions [5].

Consequently, the slant hydrostatic and wet delays plus the gradients are added to the slope total tropospheric delay from satellite *p* to receiver *u*, which is represented as δT_u^p in Eq. (21), in this work.

$$\delta T_u^p = M_{h,u}^p \delta T_{zh,u} + M_{w,u}^p \delta T_{zw,u} + \delta T_{ns} M_{T_a}(E_u^p)cosA_u^p + \delta T_{ew} M_{T_a}(E_u^p)sinA_u^p$$

Where,

$$\mathrm{M_h} \equiv \begin{bmatrix} M_h^1 \\ M_h^2 \\ \cdot \\ \cdot \\ \cdot \\ M_h^{ns} \end{bmatrix}, M_w \begin{bmatrix} M_w^1 \\ M_w^2 \\ \cdot \\ \cdot \\ \cdot \\ M_w^{ns} \end{bmatrix} \qquad (27)$$

As a result, the tropospheric delay's double divergence can be shown as follows:

$$\begin{aligned}\delta T_{ku}^{pq} &\equiv (\delta T_k^p - \delta T_k^p) - (\delta T_k^q - \delta T_u^q) \\ &= (M_{h,k}^{pq} \delta T_{\dot{z}h,k} - M_{h,k}^{pq} \delta T_{\dot{z}h,u}) \\ &\quad - (M_{w,k}^{pq} \delta T_{zh,k} - M_{w,u}^{pq} \delta T_{zh,u}) \\ &\quad + (M_{w,k}^{pq} \delta T_{z,k} - M_{w,u}^{pq} \delta T_{z,u}) \\ &\quad + \left(M_{T_{ns,k}}^p \delta T_{ns,k}^p + M_{T_{ew,k}}^p \delta T_{ew,k}^p\right) \\ &\quad - \left(M_{T_{ns,u}}^p \delta T_{ns,u}^p - M_{T_{ew,u}}^p \delta T_{ew,u}^p\right) \\ &\quad - \left(M_{T_{ns,k}}^q \delta T_{ns,k}^q + M_{T_{ew,k}}^q \delta T_{ew,k}^q\right) \\ &\quad - \left(M_{T_{ns,u}}^q \delta T_{ns,u}^q - M_{T_{ew,u}}^q \delta T_{ew,u}^q\right)\end{aligned}$$

$$= (M_{h,k}^{pq} \delta T_{\dot{z}h,k} - M_{h,k}^{pq} \delta T_{\dot{z}h,u}) - (M_{w,k}^{pq} \delta T_{zh,k} - M_{w,u}^{pq} \delta T_{zh,u}) + (M_{w,k}^{pq} \delta T_{z,k} - M_{w,u}^{pq} \delta T_{z,u}) + \left(M_{T_{ns,k}}^{pq} \delta T_{\dot{n}s,k} + M_{T_{ns,u}}^{pq} \delta T_{\dot{n}s,u}\right) + \left(M_{T_{ew,k}}^{pq} \delta T_{\dot{e}w,k} + M_{T_{ew,u}}^{pq} \delta T_{\dot{e}w,u}\right)$$

$$\text{Where,} \quad M_{T_{ns,*}} = \begin{bmatrix} M_{az}^1 \cos A_*^1 \\ M_{az}^2 \cos A_*^2 \\ \cdot \\ \cdot \\ \cdot \\ M_{az}^{ns} \cos A_*^{ns} \end{bmatrix}, \quad M_{T_{ew,*}} = \begin{bmatrix} M_{az}^1 \cos A_*^1 \\ M_{az}^2 \cos A_*^2 \\ \cdot \\ \cdot \\ \cdot \\ M_{az}^{ns} \cos A_*^{ns} \end{bmatrix}$$

(29)

4. Ionospheric Delay Models

NavIC positioning encounters significant error from the ionosphere, posing a challenge especially for single-frequency users who lack the option of an ionosphere-free combination. As outlined in section 1, existing ionospheric models are not robust enough to address this issue adequately. Hence, our research focuses on utilizing inhomogeneous mapping functions to estimate and rectify ionospheric delays.

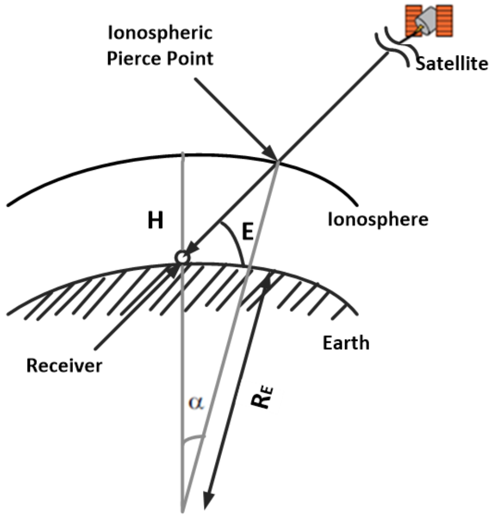

Figure 2. Single layer model for ionospheric delay

4.1 Ionospheric Delay

Expressing the slant ionospheric delay $\delta I_u^p(E_u^p)$ involves utilizing the zenith ionospheric delay (ZID) δI_u^p and a mapping function $M_{I,u}(E_u^p)$ $\delta I_{\cdot z,u}$ as shown below:

$$\delta I_u^p = M_{I,u}(E_u^p) \delta I_{\cdot z,u} \qquad (30)$$

Where,

$$M_{I,u}(E_u^p) = \frac{1}{\sqrt{1-(\frac{R_E}{R_E+H} cosE_u^p)^2}} \quad (28) \qquad (31)$$

In this context, we apply the single-layer model illustrated in Fig. 2. The term RE (approximately 6,371 kms) represents the mean earth radius, while *H* signifies the height of the single layer.

4.2 Ion-Sphere Difference

In the preceding section, we enhanced the modeling of tropospheric delays by incorporating their gradients to improve accuracy. In a similar vein, modelling ionospheric delays can be accomplished through the use of gradients. The extension attributed to ionospheric gradients can be represented as per [11-13].

$$\delta I_{G,u}(E_u^p, A_u^p) = \delta I_{ns,u} M_{I,u}(E_u^p) cotE_u^p cosA_u^p + \delta I_{ew,u} M_{I,u}(E_u^p) cotE_u^p sinA_u^p \qquad (32)$$

This investigation, the eastward and northward horizontal gradients, denoted as $I_{ns,u}$ and $I_{ew,u}$ respectively, are considered alongside the inhomogeneous mapping functions $M_{I,u}(E_u^p)\cot E_u^p \cos E_u^p$ *and* $\mathrm{MI,u}(E_u^p)\cot E_u^p \sin A_u^p$. The slant ionospheric delay, denoted as δI_u^p in Eq. (30), between the satellite p and receiver u is thus replaced with.

$$\delta I_u^p = M_{I,u}\left(E_u^p\right)\delta I_{z,u} + \delta I_{G,u}^p\left(E_u^p, A_u^p\right) \tag{33}$$

In this work, we tackle an assessment of ionospheric delays by taking into account the gradients and the zenith delay of the individual ionosphere single discrepancies between two receiver stations as unknown parameters. The ionospheric total delay can be expressed in the following way:

$$\begin{aligned}\delta I_{ku}^{pq} &= \left(\delta I_k^p - \delta I_u^p\right) - \left(\delta I_k^q - \delta I_u^q\right)\\ &= \left\{\left(M_{I,k}^p\delta I_{z,k}^p + \delta I_{G,k}^p\right) - \left(M_{I,u}^p\delta I_{z,u}^p + \delta I_{G,u}^p\right)\right\} - \left\{\left(M_{I,k}^q\delta I_{z,k}^q + \delta I_{G,k}^q\right) - \left(M_{I,u}^q\delta I_{z,u}^q + \delta I_{G,u}^q\right)\right\}\text{-}\\ &= \left(M_{I,k}^p\delta I_{z,k}^p + M_{F_{ns,k}}^p\delta I_{ns,k}^p + M_{F_{ew,k}}^p\delta I_{ew,k}^p\right)\\ &\qquad - \left(M_{I,u}^p\delta I_{z,u}^p + M_{F_{ns,u}}^p\delta I_{ns,u}^p + M_{F_{ew,u}}^p\delta I_{ew,u}^p\right)\\ &\qquad - \left(M_{I,k}^q\delta I_{z,k}^q + M_{F_{ns,k}}^q\delta I_{ns,k}^q + M_{F_{ew,k}}^q\delta I_{ew,k}^q\right)\\ &\qquad + \left(M_{I,u}^q\delta I_{z,u}^q + M_{F_{ns,u}}^q\delta I_{ns,u}^q + M_{F_{ew,u}}^q\delta I_{ew,u}^q\right)\\ &\approx M_{I,k}^p\delta I_{z,k}^p - M_{I,k}^q\delta I_{z,k}^q + M_{F_{ns,k}}^{pq}\delta I_{\dot{n}s,k} + M_{F_{ew,k}}^{pq}\delta I_{\dot{e}w,k} - M_{F_{ns,u}}^{pq}\delta I_{\dot{n}s,u} + M_{F_{ew,u}}^{pq}\delta I_{\dot{e}w,u}\end{aligned} \tag{34}$$

Where

$$M_{F_{ns,u}}^{pq} = M_*^p cot E_*^p cos A_*^p \tag{35}$$

$$M_{F_{ew,u}}^{pq} = M_*^p cot E_*^p cos A_*^p \tag{36}$$

Here, $\delta I_{z,}^p$ represents the zenith delay, and MF is the mapping function that converts $\delta I_{\dot{z}}$ into the delay along the path. $\delta I_{\dot{n}s}$ and $\delta I_{\dot{e}w}$ are the ionospheric gradient vectors-oriented north-south and east-west respectively.

4.3. Observation Equation

The observed equation can be expressed as follows by straightening the observing equations (Eqs.1-4) and updating the tropospheric and ionospheric delays [14-16]:

$$\begin{bmatrix}\tilde{\rho}_{CA,uk}^{pq}\\ \tilde{\rho}_{PY,uk}^{pq}\\ \tilde{\emptyset}_{L1,uk}^{pq}\\ \tilde{\emptyset}_{L2,uk}^{pq}\end{bmatrix} = \begin{bmatrix}\rho_{CA,uk}^{pq}\\ \rho_{PY,uk}^{pq}\\ \emptyset_{L1,uk}^{pq}\\ \emptyset_{L2,uk}^{pq}\end{bmatrix} - \left[r_{\tilde{u}^{(j)}k}^{pq} + g_{\tilde{u}^{(j)}k}^{pq}(-\tilde{u}^{(j)}\right] \\ -\left[(M_{h,k}^{pq}\delta T_{\dot{z}h,k} - M_{h,u}^{pq}\delta T_{\dot{z}h,u})\right] \\ - \left[(M_{w,k}^{pq}\delta T_{\dot{z}h,k} - M_{w,u}^{pq}\delta T_{\dot{z}h,u})\right] \tag{37}$$

Using Eqs. (28), (33), and (36), the observation equation can be formulated as follows:

$$y_t = H_t\theta_t + v_t \tag{38}$$

Where

$$y \equiv [\tilde{\rho}_{CA}^T, \tilde{\rho}_{PY}^T, \tilde{\emptyset}_{L1}^T, \tilde{\emptyset}_{L2}^T]^T \tag{39}$$

$$H \equiv [A, B, C, D]^T \tag{40}$$

$$\theta = [u^T, \delta I^T, \delta T^T, \lambda 1 N_{L1}^T, \lambda 2 N_{L2}^T]^T \tag{41}$$

$$v = [e_{CA}^T, e_{PY}^T, \delta T^T, \lambda 1\varepsilon_{L1}^T, \lambda 2\varepsilon_{L2}^T]^T \tag{42}$$

$$u = [x_u, y_u, z_u]^T \tag{43}$$

$$A \equiv \begin{bmatrix}G\\ G\\ G\\ G\end{bmatrix} \tag{44}$$

$$B \equiv \begin{bmatrix} M_{I,k} & M_{Fns,k} & M_{Few,k} & -M_{Fns,u} & -M_{Few,u}\\ \frac{f_1^2}{f_2^2}M_{I,k} & \frac{f_1^2}{f_2^2}M_{F_{ns},k} & \frac{f_1^2}{f_2^2}M_{F_{ew},k} & -\frac{f_1^2}{f_2^2}M_{F_{ns},u} & -\frac{f_1^2}{f_2^2}M_{F_{ew},u}\\ -M_{I,k} & -M_{Fns,k} & -M_{Few,k} & -M_{Fns,u} & -M_{Few,u}\\ -\frac{f_1^2}{f_2^2}M_{I,k} & -\frac{f_1^2}{f_2^2}M_{F_{ns},k} & -\frac{f_1^2}{f_2^2}M_{F_{ew},k} & -\frac{f_1^2}{f_2^2}M_{F_{ns},u} & -\frac{f_1^2}{f_2^2}M_{F_{ew},u}\end{bmatrix} \tag{45}$$

$$C \equiv \begin{bmatrix} M_{w,k} - M_{w,u} M_{T_{ns,k}} M_{T_{ew,k}} - M_{T_{ns,u}} - M_{T_{ew,u}}\\ M_{w,k} - M_{w,u} M_{T_{ns,k}} M_{T_{ew,k}} - M_{T_{ns,u}} - M_{T_{ew,u}}\\ M_{w,k} - M_{w,u} M_{T_{ns,k}} M_{T_{ew,k}} - M_{T_{ns,u}} - M_{T_{ew,u}}\\ M_{w,k} - M_{w,u} M_{T_{ns,k}} M_{T_{ew,k}} - M_{T_{ns,u}} - M_{T_{ew,u}}\end{bmatrix} \tag{46}$$

$$D \equiv \begin{bmatrix} O\,O\\ O\,O\\ I\,O\\ O\,I\end{bmatrix} \tag{47}$$

$$\delta I \equiv \begin{bmatrix} \delta I_{z,ku}^{1} \\ . \\ \delta I_{z,ku}^{ns} \\ \delta \mathrm{I}_{ns,k} \\ \delta \mathrm{I}_{ew,k} \\ \delta \mathrm{I}_{ns,u} \\ \delta \mathrm{I}_{ew,u} \end{bmatrix}; \quad \delta T \equiv \begin{bmatrix} \delta T_{z,k} \\ \delta T_{z,u} \\ \delta T_{ns,k} \\ \delta T_{ew,k} \\ \delta T_{ns,u} \\ \delta T_{ew,u} \end{bmatrix} \tag{48}$$

G is a partial differentiator coefficient Procession

$$G \equiv \left[g_{\tilde{u}(j)}^{12}, \quad g_{\tilde{u}(j)}^{13} \quad \cdot \quad \cdot \quad g_{\tilde{u}(j)}^{1ns} \right]^{T} \tag{49}$$

5. Kalman Filter

To estimate the unknown vector θ, the Kalman filter is employed. The measurement equations presented in equation (37), along with the state equation, can generally be expressed as follows:

$$\theta_{t+1} = F\theta_t + w_t \quad t = 0,1,2,\ldots.., \tag{50}$$

Here, F is a known matrix with appropriate dimensions. The Kalman filter is based on the assumption that the disturbances w_t and θ_t are white Gaussian processes, as follows [17]: Hence, w_t and θ_t are considered to be white Gaussian processes, such that:

$$E\{w_t\} = 0, \quad E\{v_t\} = 0 \tag{51}$$

$$\mathrm{E}\left\{ \begin{pmatrix} w_t \\ v_t \end{pmatrix} \begin{pmatrix} w_s^T & v_s^T \end{pmatrix} \right\} = \begin{pmatrix} Q & 0 \\ 0 & R \end{pmatrix} \delta_{ts} \tag{52}$$

$$E\{w_t \theta_s^T\} = 0, \quad E\{v_t \theta_s^T\} = 0 \quad s \le t \tag{53}$$

$$\theta_0 \sim \aleph(\overline{x_0}, \textstyle\sum_0) \tag{54}$$

Next, the following is an example of the Kalman filter algorithm:

a) Projected and Selected Approximations

$$\hat{\theta}_{t+1|t} = F\hat{\theta}_{t|t} \tag{55}$$

$$\hat{\theta}_{t|t} = \hat{\theta}_{t|t-1} + K_t[y_t - H\hat{\theta}_{t|t-1}] \tag{56}$$

b) Filter Gain (Kalman Gain)

$$K_t = P_{t|t-1} H^T \left[H P_{t|t-1} H^T + R \right]^{-1} \tag{57}$$

c) Predicted and Filtered Error Covariance Matrices

$$P_{t+1|t} = F P_{t|t} F^T + Q \tag{58}$$

$$P_{t|t} = P_{t|t-1} - K_t H P_{t|t-1} \tag{59}$$

d) Initial Conditions

$$\hat{\theta}_{0|-1} = \bar{\theta}_0, P_{0|-1} = \textstyle\sum_0 \tag{60}$$

6. Experimental Set up and Results

The proposed positioning algorithms were tested using real time data from four receiver stations: AGRL, UCE, OU, Hyderabad, STA2 Hyderabad, CBIT, Hyderabad and KNL, India. These stations' coordinates are listed in Table 1. The estimating techniques used are technique 1: Ionospheric + Tropospheric zenith delays and technique 2: Ionospheric+ Tropospheric delays with gradients. The results obtained using technique 1 are indicated in the following sections as red colour line, whereas results obtained using method 2 are displayed as blue colour line.

Table 1: The coordinates of receiver stations

S.No.	Station Name	Latitude (deg)	Longitude (deg)
1	AGRL	17.4076^0 N	78.5175^0E
2	STA	17.4172^0 N	78.5509^0E
3	CBIT	17.3921^0N	78.3195^0E
4	KNL	15.79^0N	78.07^0E

6.1 Results

As shown in Table 2, the experiment made use of two different approaches and three datasets. To avoid multipath and other impacts on data points, an elevation angle less than 20 degrees were eliminated from all datasets using an elevation cut-off filter. Accord systems GPS/IRNSS/GAGAN receiver fitted with multi band antenna was utilized by every ground station. At 1 Hz sampling rate observations were acquired by these receivers, along with the L5 and S1 carrier phases.

Table 2: Details of experiments and dataset collected

Dataset	Station		Experiment Date and Time
A	Rover	STA1	

	Reference station	AGRL	September 20 &21, 2022 (0:00 – 23:59:59)
	Baseline length	3.701 kms	
B	Rover	CBIT	
	Reference station	AGRL	
	Baseline length	21.08 kms	
C	Rover	KNL	
	Reference station	AGRL	
	Baseline length	186.082 kms	

6.2 Results for the 3.701[km] baseline using Dataset A

The results for dataset A, which has a short baseline of only 3.701 kilometers, are shown in Fig.3. The red colour line and blue colour line represent positioning error in East, North, and Up axes using method1 and method2. The error is computed by subtracting the estimated positions from the reference position coordinates given in Table 1. The root mean square error (RMSE), standard deviation, and mean of error details of the positioning results are compiled in Table 3. The temporal range that the data analysis examines in this figure is 86400 seconds. Fig.3 shows error in east, north and up direction is highly dynamic during the initial period of time, later it has become almost constant.

From the results, it shows that positioning error in Up direction is more compared to east and north directions. Moreover, method 2 is reducing the RMS of position error from 0.0368m to 0.0135m (Table 3).

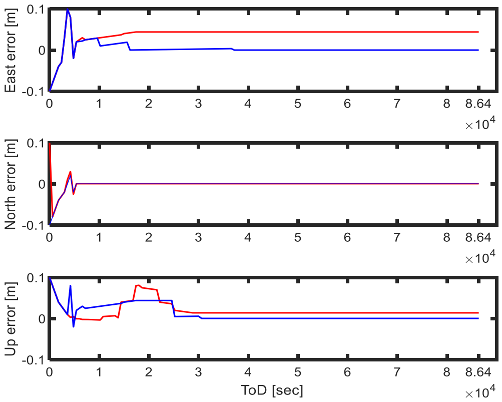

Figure 3. Error in ENU coordinates for 3.701 kms base line measurements

Table 3. Statistics of error in ENU coordinates for 3.701 kms base line measurements

S.No.	Method	Direction	Error(m)	Std.(m)	RMS(m)
1	Method1	E	0.0300	0.0059	0.0315
		N	-0.0005	0.0016	0.0016
		U	-0.0301	0.0194	0.0368
2	Method2	E	0.0027	0.0028	0.0044
		N	0.0006	0.0012	0.0012
		U	0.0098	0.0107	0.0135

6.3 Results for the 21.08 kms baseline using Dataset B

Fig. 4 presents the results for a medium baseline of 21.08 kilometers, which brings us back to dataset B. As indicated in the previous figure, the positioning error in local level axes (East, North, and Up) is shown by red line and blue line. As previously, the estimated positions were differenced by the reference positions listed in Table 1 to determine these inaccuracies. Let's now look at Fig. 4, which shows the Easting, Northing, and Up (ENU) errors for a 21.08 kilometer longer baseline.

The positioning error results statistics are summed up in Table 4. The data under analysis covers a time interval of 86400 seconds.

From Fig.4, it is noticed that method 1 and method 2 performance in North direction is approximately same, and RMS error is more in Up direction as indicted in the short baseline results (Table 4).

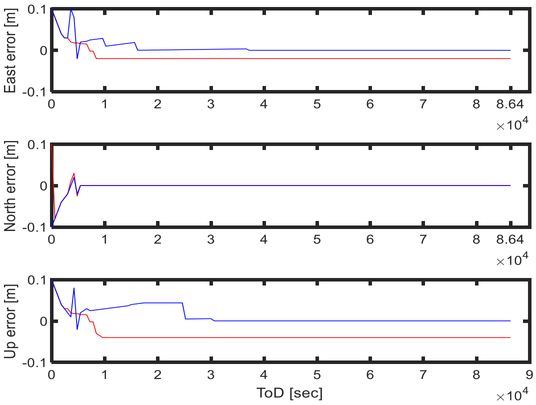

Figure 4. Error in ENU coordinates for 21.08 kms base line measurements

Table 4. Statistics of error in ENU coordinates for 21.08 kms base line measurements

S.No.	Method	Direction	Error (m)	Std. (m)	RMS(m)
1	Method1	E	-0.0013	0.0026	0.0105
		N	0.0006	0.0014	0.0013
		U	-0.0024	0.0128	0.0246
2	Method2	E	0.0012	0.0018	0.0021
		N	0.0005	0.0015	0.0076
		U	0.0040	0.0057	0.0084

6.4 Results for the 186.082 kms baseline using Dataset C

The results for dataset C, which has the longest baseline at 186.082 kilometers, are likewise displayed in Figure 5. In keeping with the earlier representations, the local East, North, and Up axes positioning errors are shown by blue lines and red lines. These errors were calculated, much like for the other datasets, by subtracting the estimated positions from the reference positions given in Table 1. Table 5 provides statistics of positioning error results for dataset C. It's crucial to remember that the dataset's analyzed data spans from 0 to 86400 seconds.

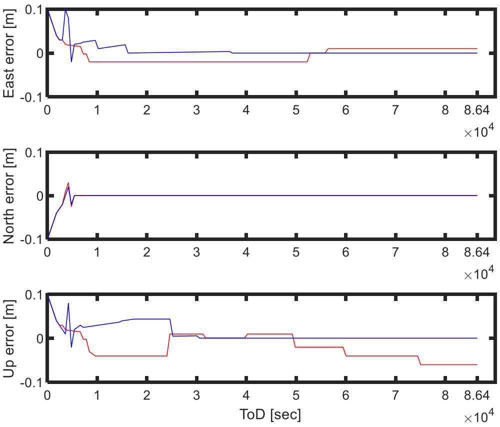

Figure 5. Error in ENU coordinates for 186.082 kms base line measurements

Table 5. Statistics of error in ENU coordinates for 186.082 kms base line measurements

S.No.	Method	Direction	Error (m)	Std.(m)	RMS(m)
1	Method1	E	-0.0078	0.0146	0.0162
		N	0.0013	0.0037	0.0038
		U	-0.0295	0.0419	0.0489
2	Method2	E	0.0015	0.0051	0.0057
		N	0.0014	0.0043	0.0034
		U	-0.0148	0.0156	0.0196

The results of the studies showed that focusing on the delays of the ionospheric and tropospheric gradients across different baselines was very useful for calculating them. This was particularly useful for the ionosphere, which has a tendency to be highly active.

7. Conclusions

The relative positioning methods that were presented in this paper estimate the gradients of ionospheric and tropospheric delays. Further, the Kalman filter is used to implement the proposed methods. The algorithms are tested with real-time data of NavIC receiver stations of different base line lengths. For all baseline length short, medium and long baseline lengths RMS (in meters) is high in up direction using method1 and method2. According to our experimental findings, the suggested technique with gradient estimation produces more accurate position than those without it when operating in static situations.

References

[1] K.C.T. Swamy, Venkata Ratnam Devanaboyina, Towseef Ahmed Shaik, Double difference method with zero and short base length carrier phase measurements for Navigation with Indian Constellation satellites L5 (1176.45 MHz) signal quality analysis, International Journal of Satellite Communications and Networking, 40(4), 294-304, 2022.

[2] K.C.T. Swamy, D Venkata Ratnam, T Suman, S Towseef Ahmed, Time-differenced double difference method for measurement of Navigation with Indian Constellation (NavIC) receiver differential phase bias, Measurement, 207, 112385, 2023.

[3] K.C.T. Swamy, Global navigation satellite system and augmentation, Resonance, 22, 1155-1174, 2017.

[4] C. Uratani, K. Sone, Y. Muto, S. Maruo and S. Sugi¬moto: Dynamical Models for Carrier-Phase Kinematic GPS Positioning, Proc. 16th Int. Tech. Meeting of the Satellite Division of the Institute of Navigation (ION GPS/GNSS 2003), pp. 809-818, Portland, OR, Sep., 2003.

[5] Y. Muto, Y. Kubo, C. Uratani and S. Sugimoto: New Dynamical Models for Kinematic GPS Positioning, Proc. 17th Int. Tech. Meeting of the

Satellite Division of The Institute of Navigation (ION GNSS 2004), pp. 2519-2528, Long Beach, CA, Sep., 2004.

[6] K.C.T. Swamy, AD Sarma, V Satya Srinivas, P Naveen Kumar, PVD Somasekhar Rao, Accuracy evaluation of estimated ionospheric delay of GPS signals based on Klobuchar and IRI-2007 models in low latitude region, IEEE Geoscience and Remote Sensing Letters, 10,6, 1557-1561, 2013.

[7] T. Yanase, S. Fujita, H. Tanaka, Y. Kubo and S. Sugimoto: Long Baseline GNSS Relative Positioning with Estimating Zenith Delays of Ionospheric and Tro¬pospheric Delays, Proc. International Symposium on GPS/GNSS 2009, pp. 185, Jeju, Nov., 2009.

[8] K. Nishikawa, S. Fujita, Y. Kubo and S. Sugimoto: PPP based on GR Models with Estimating Tropo¬spheric and Ionospheric Delays, Proc. 22th Int. Tech. Meeting of the Satellite Division of The Institute of Navigation (ION GNSS 2009), pp. 2496-2507, Savan¬nah, Georgia, Sep., 2009.

[9] E. K. Smith and S. Weintraubz: The constants in the equation for atmospheric refractive index at radio fre¬quencies, Proc. IRE, Vol. 41, pp. 1035-1037, 1953.

[10] B. W. Parkinson and J. J. Spilker Jr.(Eds.): Global Po¬sitioning System: Theory and Applications, Vol. I, II, AIAA, Washington, DC, 1997.

[11] P. Misra and P. Enge: Global Positioning System Signals, Measurements, and Performance, Second Edi¬tion, Ganga-Jamuna Press, Massachusetts, 2006.

[12] S. Sugimoto, Y. Kubo and H. Kumagai: GPS Navi¬gation Algorithms and Estimation - Detection Theory, Systems, Control and Information ISCIE, Vol. 46, No. 5, pp. 276-285, 2002 (in Japanese).

[13] B. Hofmann-Wellenhof, H. Lichtenegger and J. Collins: Global Positioning System Theory and Prac¬tice, fifth, revised edition, Springer-Verlag, New York, 2001.

[14] K. Chen and Y. Gao. Ionospheric Effect Mitigation for Real-Time Single-Frequency Precise Point Posi¬tioning, of The Institute of Navigation , Vol. 55, No.3, pp. 205-213, Fall 2008.

[15] Devireddy Kavitha, and Perumalla Naveen Kumar, "Performance Evaluation of Global Ionospheric Models with Indian Regional Navigation Data Over Low Latitude Station During Low Solar Activity Year 2017," Progress In Electromagnetics Research C, Vol. 114, 279-295, 2021.

[16] Devireddy K, Narsetty S. Ramavath AK, Perumalla NK, "Validation of the IRI-2016 Model with Indian NavIC data for Future Navigation Applications", IET Radar Sonar Navigation International Journal. 2021; 15:37-50.

[17] R. G. Brown and P. Y. C. Hwang: Introduction to Ran¬dom Signals and Applied Kalman Filtering, third edi¬tion, John Wiley & Sons, New York, 1997.